International Journal of Modern Engineering Research (IJMER)
www.ijmer.com Vol.2, Issue.5, Sep-Oct. 2012 pp-3962-3972 ISSN: 2249-6645

An Individual Channel Designing For Integrated Multi-Port Dc-Dc Converter for Renewable Energy Applications

Devanaboyina S Singh[1], Vargil Kumar[2], D Srinivasa Rao[3]
[1](PG Scholar, Department of EEE, Gudlavaleru college of Engg / Jntuk, gudlavaleru, AP, India)
[2](Assoc Prof, Department of EEE, Gudlavaleru college of Engg/ Jntuk, India)

ABSTRACT: This paper proposes a novel converter topology that Interfaces four power ports: two sources, one bidirectional storage port, and one isolated load port. The proposed four-port dc/dc converter is derived by simply adding two switches and two diodes to the traditional half-bridge topology. Zero-voltage switching is realized for all four main switches. Three of the four ports can be tightly regulated by adjusting their independent duty-cycle values, while the fourth port is left unregulated to maintain the power balance for the system. In this a new control method individual channel designing is implemented to get efficient results, the simulation results are shown below.

Keywords**:** *DC–DC converter, half-bridge, multiple-input Single-output (MISO), multiport, zero-voltage switching (ZVS).*

I. INTRODUCTION

As interest in renewable energy systems with various sources becomes greater than before, there is a supreme need for integrated power converters that are capable of interfacing, and concurrently, controlling several power terminals with low cost and compact structure. Meanwhile, due to the intermittent nature of renewable sources, a battery backup is normally required when the ac mains is not available. This paper proposes a new four-port-integrated dc/dc topology which is suitable for various renewable energy harvesting applications. An application interfacing hybrid photovoltaic (PV) and wind sources, one bidirectional battery port, and an isolated output port is given as a design example. It can achieve maximum power-point tracking (MPPT) for both PV and wind power simultaneously or individually, while maintaining a regulated output voltage. Compared to the effort spent on the traditional two-port converter, less work has been done on the multiport converter. But, due to the advantages like low cost and compact structure, multiport converters are reported to be designed for various applications, such as achieving three bus voltages of 14 V/42 V/H.V. (high voltage of around 500 V) in electric vehicles or hybrid electric vehicles interfacing the PV panel systems PV energy harvesting with ac mains or the battery backup hybrid fuel cell and battery systems, and hybrid ultra capacitor and battery systems. From the topology point of view, multi input converters based on buck, boost, and buck–boost topologies have been reported in. The main limitation of these configurations is the lack of a bidirectional port to interface storage device.

Multiport converters are also constructed out of a multi winding transformer based on half-bridge or full bridge topologies. They can meet isolation requirement and also have bidirectional capabilities. However, the major problem is that they use too many active switches, in addition to the bulky transformer, which cannot justify the unique features of low component count and compact structure for the integrated multiport converter. The proposed four-port dc/dc converter has bidirectional capability and also has one isolated output. Its main components are only four main switches, two diodes, one transformer, and one inductor. Moreover, zero-voltage switching (ZVS) can be achieved for all main switches to allow higher efficiency at higher switching frequency, which will lead to more compact design of this multiport converter. The control design is also investigated based on the modeling of this modified half-bridge topology. In addition, a decoupling network is introduced to allow the separate controller design for each power port. Finally, a prototype has been built to verify the four-port converter's circuit operation and control capability. The proposed converter is a valuable candidate for low-power renewable energy harvesting applications.

The toolbox is inspired on a new approach for multivariable control systems, referred as Individual Channel Design (ICD). ICD is a novel analytical framework that allows the analysis and synthesis of multivariable control systems under the context of the Multivariable Structure Function (MSF) by applying classical techniques based on the Bode and Nyquist plots. With the help of this framework it is possible to investigate the potential and limitations for feedback design of any multivariable linear time–invariant control system. Although ICD is in principle a feedback structure based on diagonal controllers, it can be applied to any cross coupled multivariable system. It is based on the definition of individual transmission channels. In this context the control design is an interactive process that involves the required specifications, plant characteristics, and the multivariable feedback design process itself. Once the channels are defined it is possible to form a feedback loop with the compensator specially designed to meet *customer* specifications. In this manner the multivariable control design problem is reduced to the design of a single–input single–output control for each channel [4,5]. ICD has been reported in some control strategies, such as in small scale power networks with embedded generation [2], in the automotive and the aerospace industry [6]. So far, this toolbox has been used in different control tasks, from induction motors [9,10], synchronous generators [11], to submarines [7].

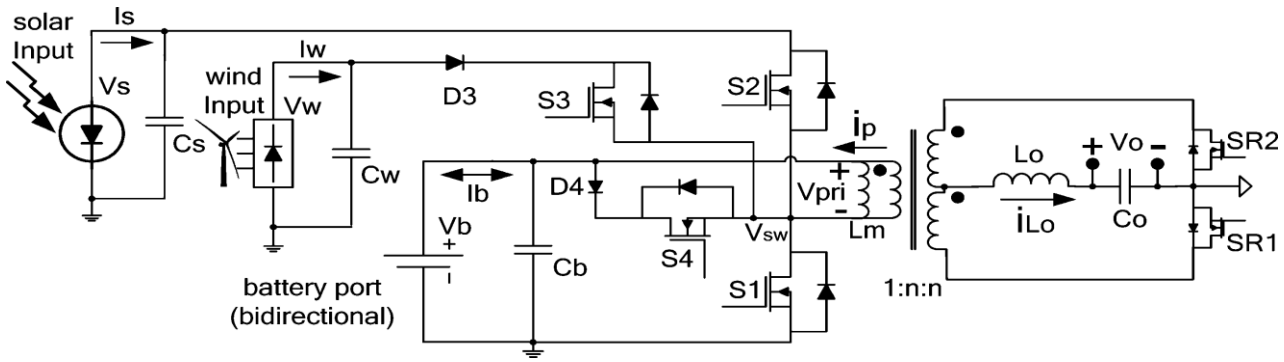

Fig. 1. Four-port half-bridge converter topology, which can achieve ZVS for all four main switches (*S*1 , *S*2 , *S*3, and *S*4) and adopts synchronous rectification

for the secondary side to minimize conduction loss.

II. Topology And Circuit Analysis

The four-port topology is derived based on the traditional two-port half-bridge converter, which consists of two main switches *S*1 and *S*2 . As shown in Fig. 1, one more input power port can be obtained by adding a diode*D*3 and an active switch *S*3 . Another bidirectional power path can be formed by adding a freewheeling branch across the transformer primary side, consisting of a diode *D*4 and an active switch *S*4 . As a result, the topology ends up with four active switches and two diodes, plus the transformer and the rectification circuit. The proposed converter topology is suitable for a number of power-harvesting applications, and this paper will target the hybrid PV wind application. It should be noted that since the wind turbine normally generates a three phase ac power, an ac/dc rectifier needs to be installed before this four-port dc/dc interface and after the wind turbine output. And then rectification stage can utilize either active power factor correction (PFC) or passive PFC. However, the ac/dc solution is beyond the scope of this paper.

2.1. Driving Scheme

Fig. 2 illustrates a possible modulation approach to realize the constant frequency pulse width modulation (PWM) control, Where *V*sawtooth is the sawtooth carrier waveform for modulation, *V*c1 , *V*c2 , and *V*c3 are control voltages derived from the voltage or current feedback controllers. By modulating these control voltages, driving signals for *S*1 , *S*2 , and *S*3 can be generated, respectively. Then, by reversing *S*1 and *S*3 driving signals, *S*4 and two SR signals can be obtained. It should be noted that *S*2 , *S*3 , and *S*4 do not need to be gated ON at the same time; instead, *S*3 is only required to turn ON a little earlier before *S*2 turns OFF, and *S*4 is only required to turn ON a little earlier before *S*3 turns OFF. No dead time is necessary between *S*2 and *S*3 , nor between *S*3 and *S*4 ,

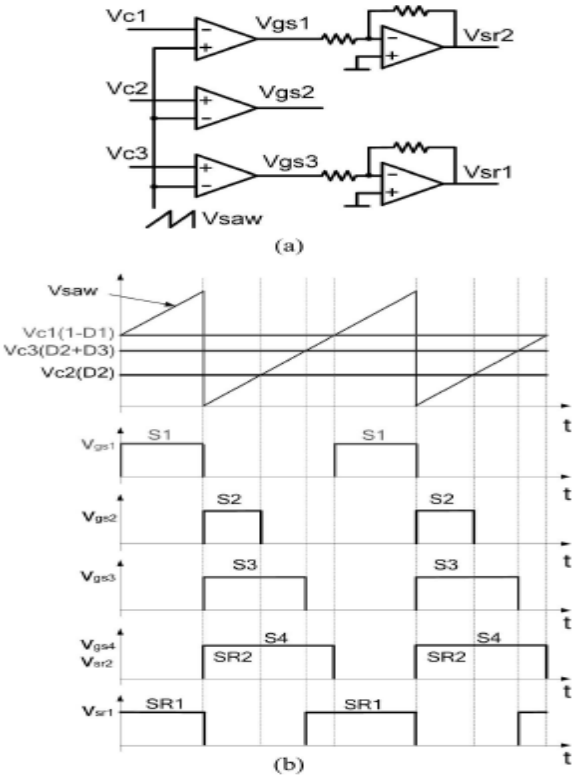

Fig. 2. Proposed modulation scheme. (a) PWMmodulation circuits. (b) Driving signal key waveforms.

because the existence of diodes can prevent shoot-through problems. But the dead time between S1 and S2 and between S1 and S4 is necessary to prevent shoot-through, and also to create ZVS conditions for S1 and S2 .

2.2 Principle of Circuit Operation

The steady-state waveforms of the four-port converter are shown in Fig. 3, and the various operation stages in one switching cycle are shown in Fig. 4. To simplify the analysis of operation, components are considered ideal, except otherwise indicated. The main operation stages are described as follows.

Stage 1 (t0–t1): Before this stage begins, the body diode of

S1 is forced on to recycle the energy stored in the transformer leakage inductor, and the output is freewheeling. At time t0, S1 is gated ON with ZVS, and then, the leakage inductor is reset to zero and reverse-charged.

Stage 2 (t1–t2): At time t1 , the transformer primary current increases to the reflected current of iLo , the body diode of SR2 becomes blocked, and the converter starts to deliver power to output.

Stage 3 (t2–t3): At time t2 , S1 is gated OFF, causing the leakage current ip to charge the S1 parasitic capacitor and discharge the S2, S3 , and S4 parasitic capacitors.

Stage 4 (t3–t4): At time t3 , the voltage across the S2 parasitic capacitor is discharged to zero, and the S2 body diode conducts to carry the current, which provides the ZVS condition for S2. During this interval, the output is freewheeling through SR1 and SR2 body diodes.

Stage 5 (t4–t5): At time t4 , S2 is gated ON with ZVS, and

then, the leakage inductor is reset to zero and reverse-charged.
The output inductor current drop from t2 to t5 is due to the leakage inductor discharge/charge.
Stage 6 (t5–t6): At time t5 , the transformer primary current increases to the reflected current of iLo , the body diode of SR1 is blocked, and the converter starts to deliver power to output.
Stage 7 (t6–t7): At time t6 , S2 is gated OFF, thus causing the leakage current ip to charge the S2 parasitic capacitor and discharge the S1 and D3 parasitic capacitors.
Stage 8 (t7–t8): At time t7 , the voltage across D3 is discharged to zero, and then, D3 conducts. S3 is gated ON before this time; therefore, S3 has natural ZVS. Output inductor current freewheels through SR2 during this period.

Stage 9 (t8–t9): At time t8 , S3 is gated OFF, thus causing the leakage current ip to charge S2 and S3 parasitic capacitors and discharge S1 and D4 parasitic capacitors.

Stage 10 (t9–t10): At time t9 , the voltage across D4 is discharged to zero and D4 conducts. Since S4 is gated ON before this time, the leakage current freewheels through D4 and S4 , so that the leakage energy is trapped. On the secondary side, output inductor current freewheels through SR1 and SR2 .

Stage 11 (t10–t11): At time t10, S4 is gated OFF, causing the trapped leakage energy to discharge the S1 parasitic capacitor and charge the S2 , S3 and S4 parasitic capacitors.

Stage 12 (t11–t12): At time t11, the voltage across S1 is discharged to zero, and the S1 body diode conducts to carry the current, which provides ZVS condition for S1. During this
Interval, the output is freewheeling. This is the end of the switching cycle.

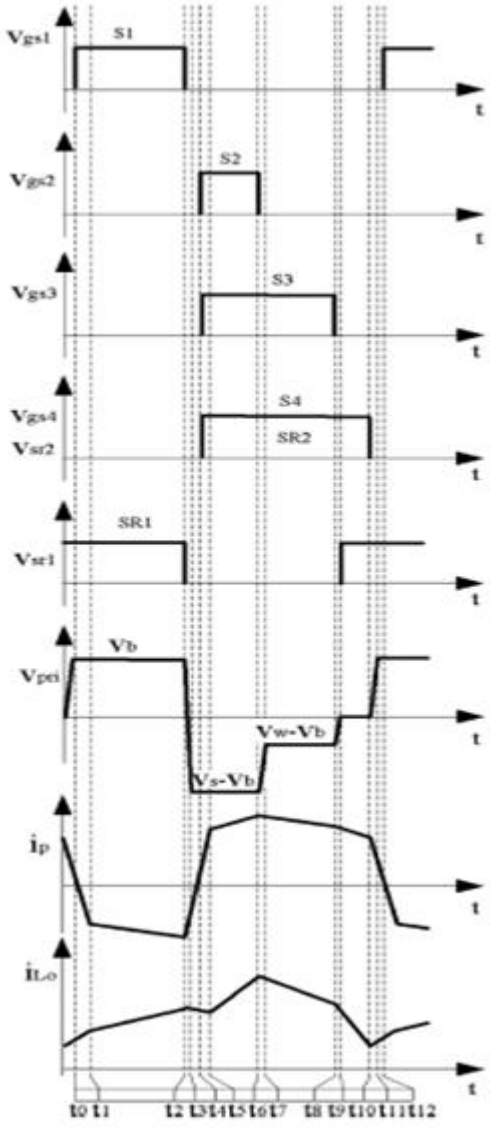

Fig. 3. Steady-state waveforms of the four-port half-bridge converter.

2.3 Steady-State Analysis

Assuming an ideal converter, the steady-state voltage governing relations between different port voltages can be determined by equating the voltage–second product across the converter's two main inductors to zero. First, using volt–second balance across the primary transformer magnetizing inductance *LM* in CCM, we have

$$V_b D_1=(V_\omega-V_b) D_2+(V_\omega-V_b)D_3 \quad (1)$$

Assuming CCM operation, the voltage-second balance across the load filter inductor *Lo* then yields

$$V_b D_1 +(V_s-V_b) D_2+(V_\omega-V_b)D_3=\frac{V_o}{n} \quad (2)$$

where *n* is the turns ratio of the transformer, *Vs* , *Vw* , *Vb* , *Vo*

are the solar input, wind input, battery, and output voltages,

respectively. The following equation is based on the power balance principle, by assuming a lossless converter, steady-state port currents can be related as follows

$$V_s I_s + V_\omega I_\omega = V_b I_b + V_o I_o \qquad (3)$$

where *Is* , *Iw* , *Ib* , *Io* are the average solar input, wind input, battery bidirectional, and load currents, respectively. The battery current *Ib* is positive during charging and negative during discharging.

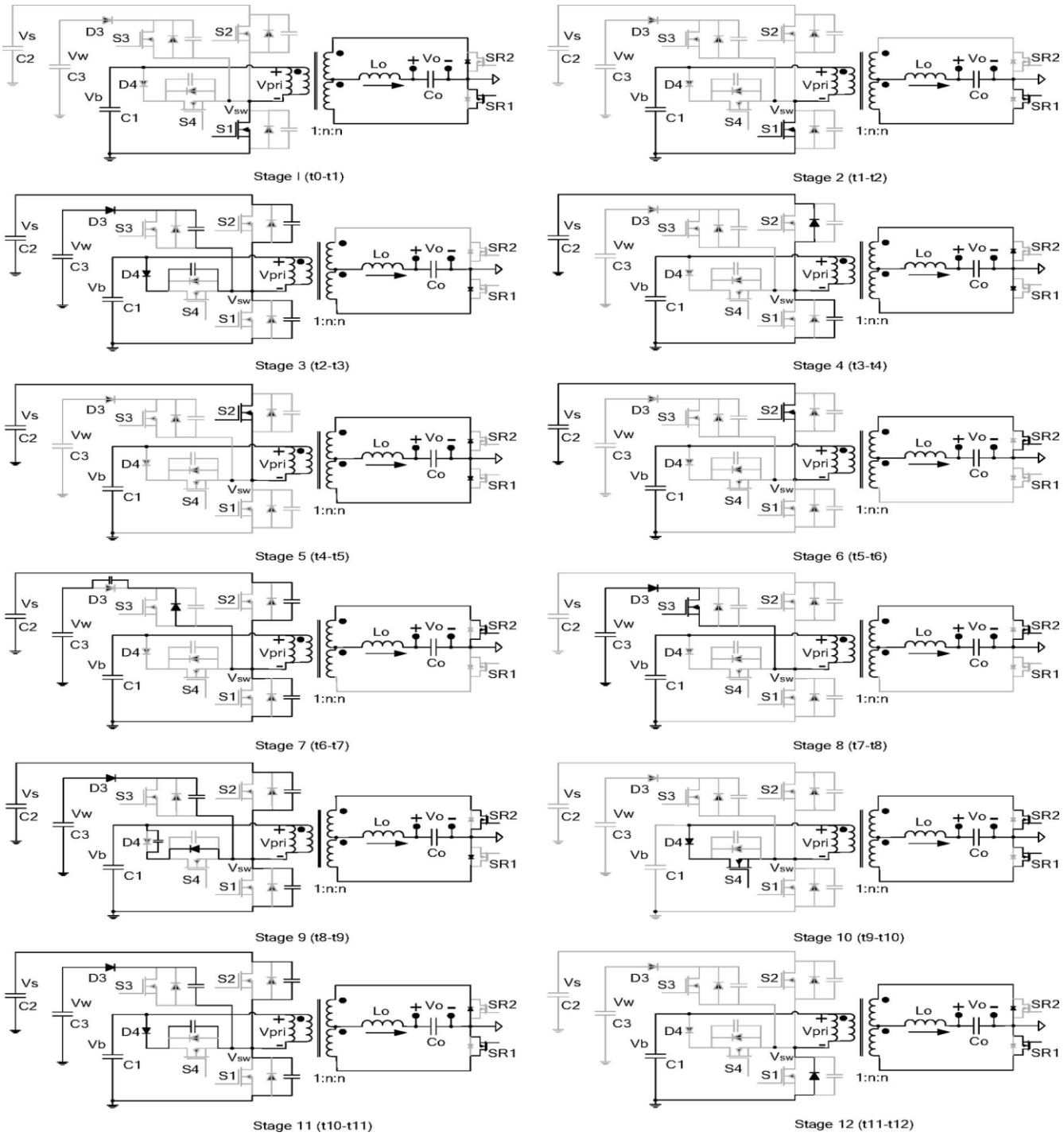

Fig. 4. Operation stages of the four-port half-bridge converter

2.4 ZVS Analysis

ZVS of the switches *S*1 and *S*2 can be realized through the energy stored in the transformer leakage inductor, while ZVS of *S*3 and *S*4 is always maintained, because the proposed will be forced on before the two switches turn ON After *S*4 is turned OFF, the leakage energy is released to discharge the *S*1 parasitic capacitor and charge *S*2 , *S*3 , and *S*4 ’s parasitic capacitors, to create the ZVS condition of *S*1. And the following condition should be satisfied as *C*oss , and *IM* is the average transformer magnetizing current, which satisfies(4)

$$\frac{1}{2} L_k (I_M + nI_o)^2 > 2Coss V_b{}^2 + Coss V_b V_s + Coss V_b V_\omega$$

$$I_M + nI_o > 0 \qquad (4)$$

where *Lk* is the transformer leakage inductance, MOSFET parasitic capacitances of *S*1 , *S*2 , *S*3 and *S*4 are assumed to be equal as *C*oss , and *IM* is the average transformer magnetizing current, which satisfies:

$$I_b = D_1(I_M + nI_o) + D_2(I_M + nI_o) + D_3(I_M + nI_o) \qquad (5)$$

Rearranging (5), we can obtain *IM* as follows:

$$I_M = \frac{I_b + (D1 - D_2 - D_3)nI_o}{(D1 + D_2 + D_3)} \qquad (6)$$

After *S*1 is turned OFF, the leakage energy will charge the *S*1 parasitic capacitor and discharge *S*2 , *S*3 , and *S*4 's parasitic
capacitors to achieve ZVS for *S*

According to (7), when the load current *Io* is small and the transformer magnetizing current *IM* is large, *IM* − *nIo*<0 cannot be met. In other words, ZVS of *S*2 will be lost. However, in most load/source conditions, ZVS of *S*2 is achievable. It should be noted that ZVS of *S*3 and *S*4 can be naturally achieved if the voltage relation *Vb*<*Vw*<*Vs* is satisfied to ensure that the paralleling diodes will always be forced on before these switches turn ON. On one hand, *Vw*< *Vs* is not difficult to meet since the solar port and wind port can be reversed if the wind port voltage *Vw* is larger than the solar port voltage *Vs*. Even if *Vw* is not always lower than *Vs* in the whole voltage ranges, the converter itself still works, but may lose some conduction period for the *S*2 branch depending on the driving overlap of *S*2 and *S*3. The solution is to change the driving scheme to avoid the *S*2 and *S*3 overlap. On the other hand, it is a step-down conversion from PV or wind port to battery port; therefore, the battery voltage *Vb* will be always lower than the PV voltage *Vs* and the wind source voltage *Vw*.

2.5. Circuit Design Considerations

When considering the semiconductor stresses, this modified half-bridge topology shows striking similarity to its traditional half-bridge counterpart. The major difference is that the transformer design of this four-port converter needs to allow for a dc current flow, and therefore, becomes similar to an inductor or a flyback transformer design. The dc biasing current rating is dictated by (6), which determines the amount of the air gap to be inserted. Other than the transformer, the circuit design and optimization technique used for the traditional half-bridge topology can be used here for this four-port topology, which provides great convenience for the practicing engineers to implement the power stage design.

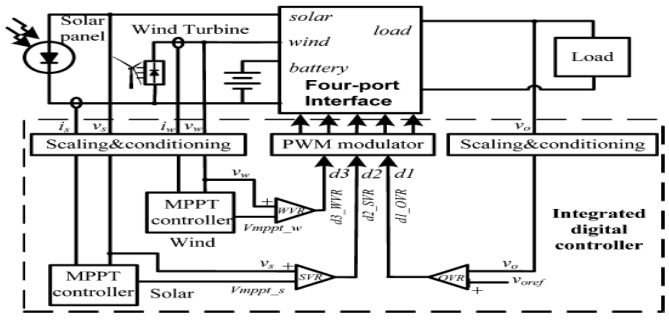

Fig. 5. Possible control structure to achieve MPPT for the PV panel and the wind turbine, meanwhile maintaining output voltage regulation. OVR, SVR, and WVR loops are to control d_1 , d_2 , and d_3 , respectively.

III. CONTROL STRUCTURE AND DYNAMIC MODELING

The proposed converter has three freedoms to control the power flow of three power ports, while the fourth port is to maintain the power balance. That means the operating point of up to three ports can be tightly regulated, while the fourth port should be left "flexible" and would operate at any point that satisfies the power balance constraints. The choice of the flexible power port dictates the feedback control layout, which is based on different control objectives. For instance, if the battery is chosen to be left "flexible," the maximal power from the solar and wind sources can be tracked by their port voltages or currents independently, and the load voltage can be regulated by a voltage feedback as well.

3.1 Control Structure

Fig. 5 shows the control structure for the hybrid PV wind system. To the three fed back controllers' icd controller are given .Three feedback controllers are as follows: a solar voltage regulator (SVR), a wind voltage regulator (WVR), and an output voltage regulator (OVR). The OVR loop is simply a voltage-feedback loop, closed around the load port, and duty cycle d1 is used as its control input. The SVR loop is used to regulate the PV panel voltage to its reference value, which is provided by an MPPT controller. And the reference value represents an estimate of the optimal operating PV voltage; duty cycle d2 is used as its control input The WVR loop is taking a very similar structure to SVR, except that its voltage reference represents the optimal operating voltage of the rectified wind turbine output voltage. The WVR loop is made to control d3 . This control strategy allows the load voltage to be tightly regulated while maximizing the PV and wind power harvesting. In this system, the battery storage plays the significant role of balancing the system energy by injecting power at heavy loads and absorbing excess power when available PV and wind power exceeds the load demand.

$$\frac{dx\hat{}(t)}{dt} = Ax\hat{}(t) + Bu\hat{}(t), \quad y\hat{}(t) = Ix\hat{}(t)$$

3.2 Dynamic Modeling:

In order to design the SVR, WVR, and OVR controllers, a small signal model of the four-port converter is desired. The detailed modeling procedure can refer to [20], which is proposed for a three-port converter. And for this four-port converter, the general modeling procedure is very similar to [20]. Therefore, to avoid unnecessary repetition, only a brief introduction is given here. First, state-space equations for five energy storage elements during the four main circuit stages are developed. For the aforementioned mode of operation, these include the solar side capacitor Cs , the wind-side capacitor Cw , the transformer magnetizing inductor LM , the output inductor Lo , and the output capacitor Co . In the next step, state-space equations in the four main circuit stages (corresponding to the turn ON of four main switches) will be averaged, and then applied with the small signal perturbation. Finally, the first-order small-signal perturbation components will be collected to form the matrices A and B, which actually represent the converter power stage model. It should be noted that the symbolic derivation of these transfer functions is fairly tedious. Alternatively, the dynamics of the plant can be calculated by

computer software like MATLAB. The resultant state-space averaging model takes the following form : (8) A

$$\begin{bmatrix} \frac{-1}{R_s C_s} & 0 & \frac{-D_2}{C_s} & \frac{-nD_2}{C_s} & 0 \\ 0 & -\frac{1}{R_w C_w} & \frac{-D_3}{C_w} & \frac{-nD_3}{C_w} & 0 \\ \frac{D_2}{L_M} & \frac{D_3}{L_M} & 0 & 0 & 0 \\ \frac{nD_2}{L_o} & \frac{nD_3}{L_o} & 0 & 0 & -\frac{1}{L_o} \\ 0 & 0 & 0 & \frac{1}{C_o} & \frac{-1}{RC_o} \end{bmatrix}$$

$$\begin{bmatrix} 0 & \frac{-I_{L_m} - (nV_o / R)}{C_o} & 0 \\ 0 & 0 & \frac{-I_{L_m} - (nV_o / R)}{C_w} \\ \frac{-V_b}{L_m} & \frac{V_a - V_b}{L_M} & \frac{V_w - V_b}{L_M} \\ \frac{nV_b}{L_o} & \frac{n(V_a - V_b)}{L_o} & \frac{n(V_w - V_b)}{L_o} \\ 0 & 0 & 0 \end{bmatrix}$$

$$\hat{u} = \begin{bmatrix} \hat{d}_1(t) \\ \hat{d}_2(t) \\ \hat{d}_3(t) \end{bmatrix}$$

where ˆ*x*(*t*) is a matrix containing the small signal state variables ˆ*vs* (*t*), ˆ*vw* (*t*), ˆ*iLm* (*t*), and ˆ*iLo* (*t*), and ˆ*vo* (*t*), ˆ*u*(*t*) is a matrix containing the control inputs ˆ *d*1 (*t*), ˆ *d*2 (*t*), and ˆ *d*3 (*t*), ˆ*y*(*t*) is a matrix containing the system outputs, and *I* is the identity matrix. With matrices *A* and *B*, transfer functions for PV, wind and output voltages to different duty-cycle values can be extracted according to (10). For example, *G*(*s*)(5,1) represents the fifth state variable *vo* and the first control variable *d*1 , thus equals to open-loop transfer function of *vo* (*s*)/*d*1 (*s*). Therefore, the row number denotes the sequence of state variable, and the column number denotes that of control input

$$G = (sI - A)^{-1} B$$
$$g_{11} = G(s)(5,1), \quad g_{21} = G(s)(1,1), \quad g_{31} = G(s)(2,1)$$
$$g_{12} = G(s)(5,2), \quad g_{22} = G(s)(1,2), \quad g_{32} = G(s)(2,2)$$
$$g_{13} = G(s)(5,3), \quad g_{23} = G(s)(1,3), \quad g_{33} = G(s)(2,3). \tag{10}$$

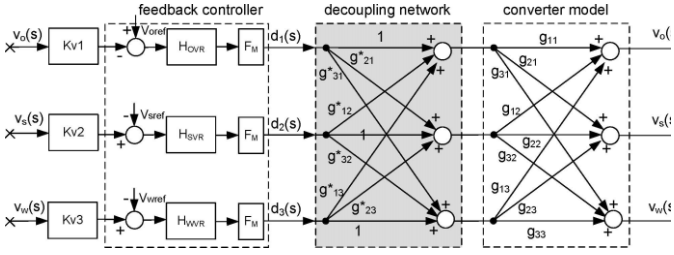

Fig. 6. Small signal model diagram, control inputs and outputs are decoupled to enable separate controller design. The far right signals are routed to the far left ones in this diagram. *Vs*ref , *Vw* ref , and *Vo* ref are the references for solar, wind and output voltages, respectively. *H*SVR ,*H*WVR, and *H*OVR are the compensators need to be designed

Fig. 6 illustrates the small signal model diagram when closing SVR, WVR, and OVR loops, which consists of the converter
model and the feedback controllers. FM represents the PWM modulator gain and different Kv values represent different voltage signal sensing gains, which can be treated as the fixed proportional values.

3.3 Decoupling Method

As can be seen from Fig. 6, the three control loops are coupled with each other, which make it difficult to design close-loop compensators for each control loop.

Therefore, a decoupling network, as shadowed in Fig. 6, is introduced, so that the control loops can be designed independently with different control-loop bandwidth requirement. Since output-port voltage regulation requirement is the most stringent of the three and the PV panel and wind turbine characteristics are relatively slower, the SVR loop is designed to have a one-decade lower bandwidth than that of OVR. Moreover, WVR bandwidth can be set to be lower than that of SVR to further reduce SVR and WVR loop interactions, since the mechanical behavior of wind blades is slower than the PV behavior of PV panels. The derivation of decoupling network G* is described as follows. The state vector matrixX can be written asX = G·U*, where U* is the modified input vector made up of duty cycles U, U* = G*·U. Therefore,X = G·G*·U. According to modern control theory, our goal is to make G·G* a diagonal matrix to allow one control input to determine one output independently. Therefore, based on G* = G^{-1} ·X·U^{-1} , the decoupling matrix G* can be derived and simplified as follows:

$$G^* \begin{bmatrix} g_{11}^* & g_{12}^* & g_{13}^* \\ g_{21}^* & g_{22}^* & g_{23}^* \\ g_{31}^* & g_{32}^* & g_{33}^* \end{bmatrix}$$

$$\begin{bmatrix} 1 & \frac{g_{13}g_{23} - g_{12}g_{33}}{g_{11}g_{33} - g_{13}g_{31}} & \frac{g_{13}g_{23} - g_{13}g_{22}}{g_{11}g_{22} - g_{12}g_{21}} \\ \frac{g_{23}g_{31} - g_{21}g_{33}}{g_{22}g_{33} - g_{23}g_{32}} & 1 & \frac{g_{13}g_{21} - g_{11}g_{23}}{g_{11}g_{22} - g_{12}g_{21}} \\ \frac{g_{21}g_{32} - g_{22}g_{31}}{g_{22}g_{33} - g_{23}g_{32}} & \frac{g_{13}g_{23} - g_{12}g_{33}}{g_{11}g_{33} - g_{13}g_{31}} & 1 \end{bmatrix}$$

It should be noted that the decoupling network is only intended to calculate and derive the separate control objects, while it does not need to be implemented in the real controller design. In other word, the decoupling can be taken as one part of the control objects, but not included in the compensators. Now, the cross-coupled three-loop control system is decoupled into three independent single-loop subsystems. The system can then be controlled using independent loop controllers and each compensator can be designed separately as well. For example, the OVR

controller can then be designed based on the following plant transfer function:

$$\frac{v_o(s)}{d_1(s)} = g_{11} + g_{12}\frac{g_{23}g_{31} - g_{21}g_{33}}{g_{23}g_{33} - g_{23}g_{32}} + g_{13}\frac{g_{21}g_{32} - g_{22}g_{31}}{g_{22}g_{33} - g_{23}g_{32}} \quad (12)$$

The open-loop OVR-loop bode plot implies that it has two main poles at around LoCo resonance, which causes a −40 dB/decade slope for gain plot while not having enough phase margin. This double pole characteristic is because that this topology is buck-type derived in terms of the output port. Therefore, the design objective is to make the gain plot pass 0 dB line at −20 dB/decade slope while maintaining a sufficient phase margin. A tradition PID controller is recommended to boost the phase. The PID compensator of HOVR takes the following form:

$$H_{OVR} = \frac{80(s/2\pi 400 + 1)(s/2\pi 500 + 1)}{s(s/2\pi 4000 + 1)(s/2\pi 5000 + 1)} \quad (13)$$

Similarly, SVR and WVR controllers can also be designed once their decoupled plant transfer functions are derived. The SVR and WVR bode plots before compensation have very high bandwidth. But the control bandwidth should be reduced to minimize loop interaction, SVR compensator HSVR is then designed to enforce relatively low control-loop bandwidth with some phase boost. There fore. a PID controller with very low gain is adopted to achieve this design goal. And WVR compensator *H*WVR is set at even lower gain to have a lower bandwidth than SVR loop. *H*SVR and *H*WVR are designed as follows: $H_{SVR} = \frac{0.08(s/2\pi 20+1)(s/2\pi 20+1)}{s(s/2\pi 1000+1)(s/2\pi 2000+1)}$ (14)

$$H_{WVR} = \frac{0.02(s/2\pi 20 + 1)(s/2\pi 30 + 1)}{s(s/2\pi 1000 + 1)(s/2\pi 1500 + 1)} \quad (15)$$

IV. INDIVIDUAL CHANNEL DESIGNING

In a typical control design task the performance is specified in terms of an output response to a given input. Meanwhile, in multivariable control, there are a number of inputs and outputs and, although it may be clear which inputs are intended to drive which outputs, the design task can be obscured by cross–coupling via the plant dynamics. Nevertheless, for clarity of both performance specification and design, it remains desirable to consider the inputs and outputs in pairs. The situation is depicted in Fig. 1, where **G** is the plant and **K** is the controller. Input ri is paired with output yi in accordance with specifications. An individual pairing is called a channel. Then, channel Ci is the pairing between ri and yi .

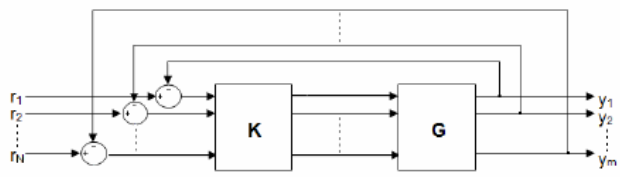

MIMO multivariable system. Channel definition

When the plant cross–coupling is weak, the design task reduces to a set of SISO design tasks and a scalar controller can be designed separately for each channel. In such context, the most appropriate methodology is to apply classical Nyquist/Bode analysis and design to each channel ICD is a framework in which Bode/Nyquist techniques can be applied directly to the channels not only when cross–coupling is weak but in all circumstances including when cross–coupling is strong. The multivariable system is decomposed into an equivalent set of SISO systems. Each SISO system is the open–loop channel transmittance between input ri and output yi, with the feedback loop between output yi and input ri open but all other feedback loops closed, for a particular choice of i. What is particular to Individual Channel Design is that the SISO channel transmittances are reformulated to make explicit the role of the plant structure. Scalar multivariable structure functions (MSFs) to which the individual channel transmittances are simply related encapsulate the significant aspects of the plant structure. The multivariable nature of the original plant is maintained in the equivalent SISO systems through the multivariable structure functions with no loss of information .The ICD set up for a 2–input 2–output plant is shown next for completeness. Let a 2x2 plant

$$\mathbf{Y}(s) = \mathbf{G}(s)\mathbf{u}(s) \quad (1)$$

be represented by

$$\begin{bmatrix} y_1(s) \\ y_2(s) \end{bmatrix} = \begin{bmatrix} g_{11}(s) & g_{12}(s) \\ g_{21}(s) & g_{22}(s) \end{bmatrix} \begin{bmatrix} u_1(s) \\ u_2(s) \end{bmatrix} \quad (2)$$

where gij(s) represents scalar transfer functions, yi(s) the outputs, and ui(s) the inputs of the system, with i,j = 1,2. If a

diagonal controller is given by

with ei(s) = ri(s) – yi(s), where ri(s) represents the plant

references, then the open loop input–output channels are

clearly defined from Figs. 2 and 3 as

$$C_i(s) = k_{ii}(s)g_{ii}(s)\left(1 - \gamma_a(s)h_j(s)\right) \quad (5)$$

where i not equal j and i,j = 1,2. The complex value d function

$$\gamma_a(s) = \frac{g_{12}(s)g_{21}(s)}{g_{11}(s)g_{22}(s)} \quad (6)$$

is referred to as the multivariable structure function (MSF).

The functions hi(s) are:

$$h_i(s) = \frac{k_{ii}(s)g_{ii}(s)}{1 + k_{ii}(s)g_{ii}(s)} \quad (7)$$

The interaction or cross coupling between the channels can be evaluated through a transfer function. For instance, the influence of channel–j on channel–i is

$$d_i(s) = \frac{g_{ij}(s)}{g_{jj}(s)}h_j(s)r_j(s) \cdot \quad (8)$$

:

It is clear that the correct interpretation of the MSF (6) is

of great importance because

- It determines the dynamical characteristics of each Input–output configuration;
- It has an interpretation in the frequency domain;
- Its magnitude quantifies the coupling between the channels (in the frequency domain);
- It is related to the plant transmission zeros (zeros of 1–a
- (s), |**G**(s)| = g11(s)g22(s) – g12(s)g21(s) = 0);a(s)=1 determines the non–minimum phase condition;
- Its closeness to (1,0) in the Nyquist plot indicates to
- What extent the plant is sensitive to uncertainty in terms of gain and phase margins. This fact plays a key role in order to obtain robust controllers.

A block diagram of the feedback system with the diagonal controller is shown in Fig. 2 and the equivalent scalar channels are shown in Fig. 3.

$$\mathbf{u}(s)=\mathbf{K}(s)\mathbf{e}(s) \qquad (3)$$

$$\begin{bmatrix} u_1(s) \\ u_2(s) \end{bmatrix}=\begin{bmatrix} k_{11}(s) & 0 \\ 0 & k_{22}(s) \end{bmatrix}\begin{bmatrix} e_1(s) \\ e_2(s) \end{bmatrix} \qquad (4)$$

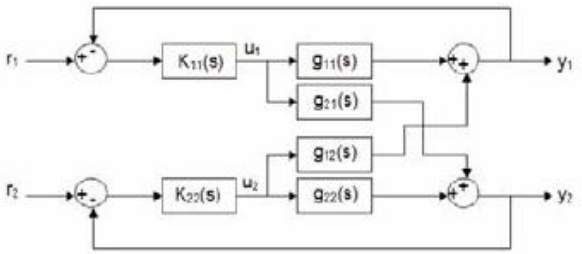

The 2-input 2-output multivariable system with a diagonal

Controller It should be emphasised that in the individual channel representation of the multivariable system there is no loss of information [4]. The multivariable character and cross coupling of the plant are contained in the MSF and the cross coupling terms. That is, (5)–(8) are equivalent to the closed loop matrix function

$$\mathbf{G}_d(s)=\left(\mathbf{I}+\mathbf{G}(s)\mathbf{K}(s)\right)^{-1}\mathbf{G}(s)\mathbf{K}(s). \qquad (9)$$

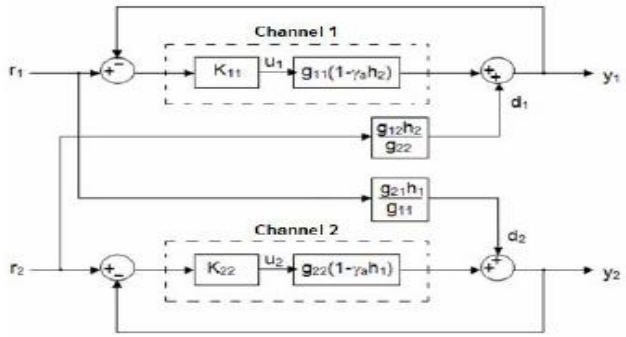

Equivalent channels of a 2-input 2-output control system It can be proven that in order to stabilise (9) it is just necessary to stabilise the channels given by (5) [8,10]. In general stabilisation of the diagonal elements of **G**(s) is not required [10]. The open loop system dynamical structure with a diagonal controller is summarised in Table I [4]. Notice that the coupling can be expressed in decibels directly from the channels (5) by means of functions a (s)hj(s). On the other hand, it is possible to determine the dynamical structure of the system using Table I and analysing the Nyquist plot of (1– a(s)hj(s)).

Table I. Dynamical structure of open loop channels

Channel	Zeros	Poles
$C_1(s)$	Zeros of $(1-\gamma(s)h_2(s))$	Poles of $g_{11}(s)$, $g_{12}(s)$, $g_{21}(s)$, $h_2(s)$
$C_2(s)$	Zeros of $(1-\gamma(s)h_2(s))$	Poles of $g_{22}(s)$, $g_{12}(s)$, $g_{21}(s)$, $h_1(s)$

It is clear that the controller performance characteristics are determined by the MSF. If the transfer matrix **G**(s) possess a non–minimum phase transmission zero, some problems will arise while stabilising it especially if the value of the zero is smaller than the desired cut–off frequency. Moreover, the robustness of the channels can be established in terms of gain and phase margins as the Nyquist paths of the functions ya(s)hi(s) do not pass near (1,0). Thus the design of kii(s), which should provide adequate gain and phase margins for kii(s)gii(s), can be obtained through an iterative process. It should be noticed that the RHPPs of the channels are RHPPs of individual transfer functions as established in Table I. On the other hand, the RHPZs of the channels are RHPZs of (1– y a(s) hi(s)). Moreover, the number of RHPZs of the previous function can be determined after applying the Nyquist Stability Criterion. In fact, the RHPZs of (1– ya (s) hi(s)) are given by where P is the number of RHPPs of □ a(s) hi(s) and N is the number of encirclements in clockwise direction to (1,0) of the complex plane in the Nyquist diagram of y a(s)hi(s). The dynamical structure of the 2x2 plant is determined by the input–output channels defined by pairing each input to each output. For instance:

$$Z=N+P. \qquad (10)$$

(a) $C_1(s)$: $u_1(s)$–$y_1(s)$ with $\gamma_a(s)=g_{12}(s)g_{21}(s)/g_{11}(s)g_{22}(s)$
$C_2(s)$: $u_2(s)$–$y_2(s)$

(b) $C_1(s)$: $u_1(s)$–$y_2(s)$ with $\gamma_b(s)=g_{11}(s)g_{22}(s)/g_{12}(s)g_{21}(s)$
$C_2(s)$: $u_2(s)$–$y_1(s)$

The coupling characteristic of each configuration is Determined from ya(s) and yb(s) –their associated MSFs.

V. SIMULATION RESULTS

In this simulation circuit three input port are taken wind ,solar and battery sources .in this four switches are used for three switches the are give duty ratios of d1,d2 and d3.the other switch is operated with duty ratio d4 which is depend on the three switches duty ratios.

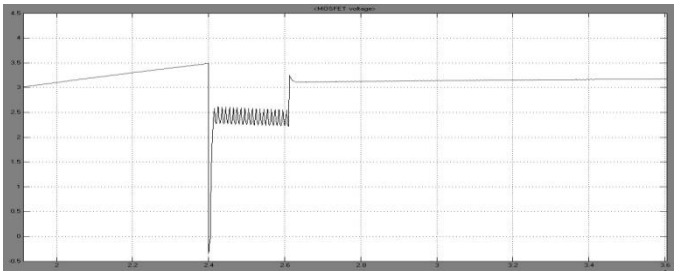

Fig.9 MOSFET voltage of S1

A four-port dc/dc converter prototype is built to verify the circuit operation. The circuit parameters are: solar port, 30– 40 V/1.5 A; wind port, 20–30 V/1.5 A; battery port, 12– 18 V/3 A; and output port, 12 V/3.3 A. The switching frequency is 100 kHz, and it is implemented by the digital control to achieve the close-loop regulation. In addition, there is no CCM and DCM transition for the output inductor current iLo , which avoids the sharp change of plant dynamic characteristics and simplifies the output-voltage feedback-controller design. The transformer magnetizing current ip is determined by both the reflected output current and the battery current.

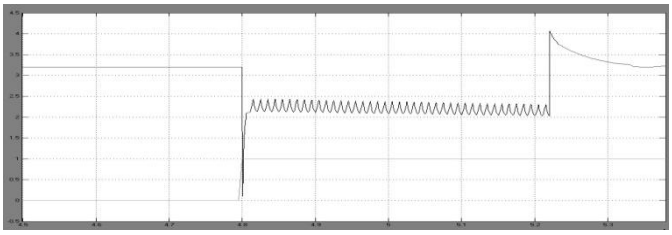

Fig.10 MOSFET voltage S1 with pulse of the switch

Fig.11 Outp

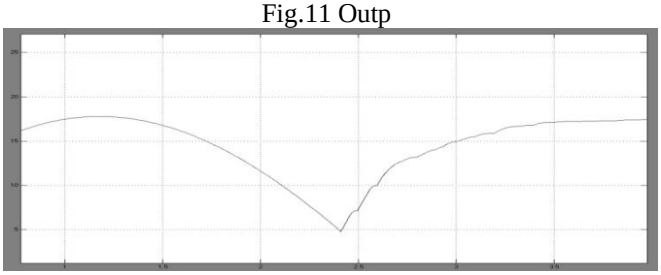

ut voltage

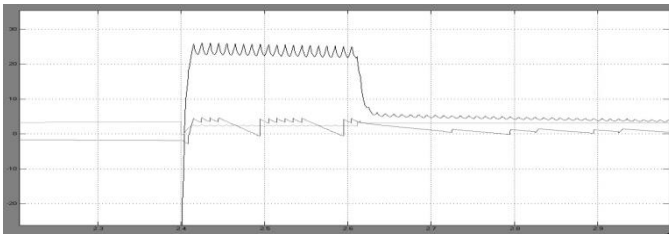

Fig.12 Out put currents ,pulse and voltage switch S1

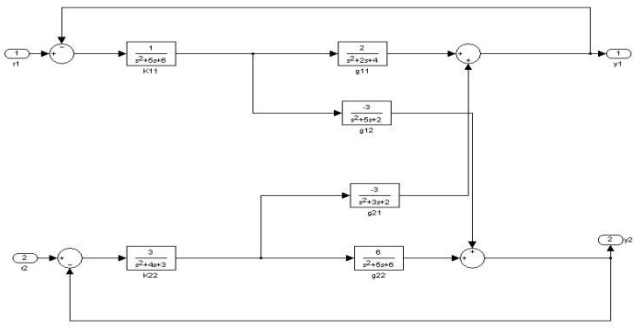

Fig.13 Icd circuit

ICD allows to coupled reference frame induction motor model. Decoupling is accomplished due to the nature of design which involves the definition individual input output channels. which are determined multi variable function s. Classical control technique (bode and nyquist) can be used to achieve multi variable control design robust variation parameter and without ripple response. Here given below bode plots of the ICD controller in bode plots of K11, K22 are represented those will be reprocess the performance of the controller transfer functions

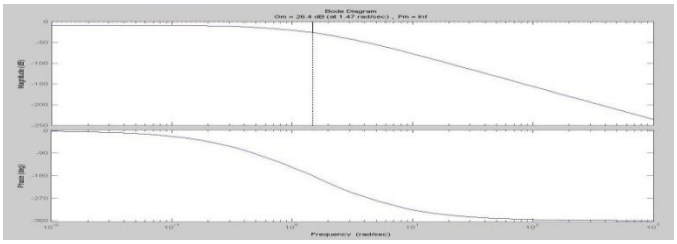

Fig.14 Bode gamma*h1

The corresponding Nyquist and Bode plots given by the toolbox are shown in Fig. 6. The user has to analyse the characteristics given in the plots, which are given next. The value of ya(0)>1 (in fact, ya(0)=2) and the Nyquist diagram of y a(s) starts at the right side of (1,0). Also, y a(s) has no RHPPs and its Nyquist path encircles clockwise the point (1,0) twice. So, according to the Nyquist Stability Criterion, (1– ya(s)) contains two RHPZs. If h2(0)>0.5 and stable then (1– ya(0)h2(0))<0. Thus, a stabilising controller k11(s) is such that k11(0)<0. On the other hand, g11(0)>0; therefore, h1(s) is unstable with one RHPP. Also, if | k11(0)g11(0) | > 0, then h1(0)>0 , if the relative degree of h1(s) is greater than the relative degree of ya(s), then y a(s)h1(s) encircles counter clockwise (1,0) once. Recall that ya(s)h1(s) has one RHPP; thus, Channel 2 is minimum–phase. **(a.4)** From **(a.3)** it is clear that the stabilising controller of Channel 2 stabilises both g22(s)(1–y a(s)h1(s)) and g22(s) simultaneously

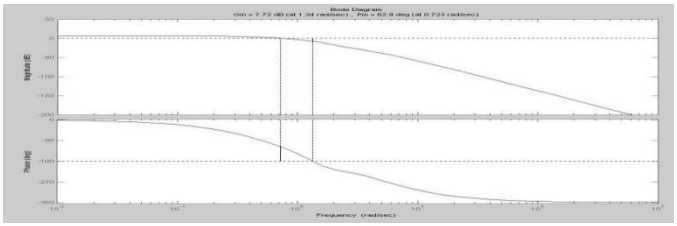

Fig.15 Bodegamma*h2

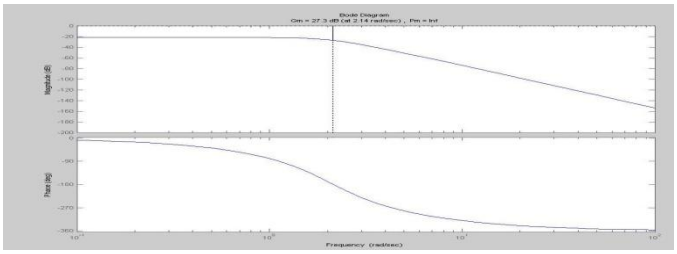

Fig.16 Bode k11

It can be concluded that the control for this configuration exists, but it presents performance limitations. the controller is designed. After performing the required iterations, the following controllers. It should be mentioned that the controller (17) satisfies the analysis carried out before. Another possible controller may exist, but the one

given before has an adequate performance (given the limitations pointed out before).

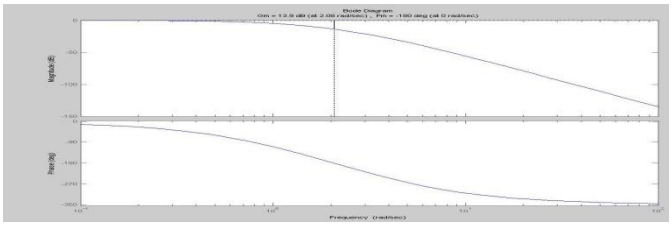

Fig.17 Bodek22

VI. CONCLUSSION

In this a four port interfacing circuit is proposed which consists of the two input source ports, a bidirectional storage port, and a galvanically isolated loading port. For the four port application to the switch ZVS technique is applied and another control technique individual channel design. Modification based on the traditional half-bridge topology makes it convenient for the practicing engineers to follow the power stage design. Three degrees of freedom necessary to control power flow in the system are provided by a four-stage constant-frequency switching sequence. This four-port converter is suitable for renewable energy systems, where the energy storage is required while allowing tight load regulation.

In this paper the novel 2x2 Individual Channel Design MATLAB® Toolbox is presented. The software is a friendly programme and a valuable aid for analysing and designing multivariable control systems. The control design for a challenging plant (non minimum phase and with strong coupling) found in literature is here developed. Some designs for 2x2 MIMO systems have been actually carried out using this toolbox, proving its adequate performance.

The toolbox saves time while designing, providing all the necessary information for every design step and allowing the assessment of controller performance throughout simulations. Structural robustness and stability margins can be considered while designing, so successful controllers can be obtained considering a possible parameter variation. Some tips are given during the design process and the instructions the designer should follow are also mentioned.

This paper has presented a novel dc/dc converter topology capable of interfacing four dc power ports: two input source ports, a bidirectional storage port, and a galvanically isolated loading port. The converter features low component count and ZVS operation for all primary switches. Modification based on the traditional half-bridge topology makes it convenient for the practicing engineers to follow the power stage design. Three degrees of freedom necessary to control power flow in the system are provided by a four-stage constant-frequency switching sequence. This four-port converter is suitable for renewable energy systems, where the energy storage is required while allowing tight load regulation.

It is suitable for low-power applications since based on the half-bridge topology, while the multiport converter based on the full-bridge topology maybe suitable for high-power applications. For the hybrid PV wind system, the proposed control structure is able to achieve maximum power harvesting for PV and/or wind power sources, meanwhile maintaining a regulated output voltage. The close-loop controller design is investigated based on the dynamic modelling of the converter power stage. Proper decoupling method is introduced to help design close-loop compensators for such a cross-coupled control system. The circuit operation of this converter and its control system is experimentally verified. Although the proposed four port converter only has two input ports, it can be extended to have n input ports. In this a control technique called ICD used for getting good optimization results of system; Individual channel designing is one of the best control techniques in upcoming control techniques. This individual channel designing implemented for 2X2 matrix .because of this one we can get out which is best output.

REFERENCES

[1] Z. Qian, O. Abdel-Rahman, and I. Batarseh, “An Integrated Four-Port DC/DC Converter for Renewable Energy Applications,IEEE Trans. Power Electron., vol. 25, no. 7, pp. 1877–1887, JULY. 2010.

[2] Y. Liu and Y. M. Chen, “A systematic approach to synthesizing multi input DC–DC converters,” IEEE Trans. Power Electron., vol. 24, no. 2, pp. 116–127, Jan. 2009.

[3] B. G. Dobbs and P. L. Chapman, “A multiple-input DC-DC converter topology,” in Proc. IEEE Power Electron. Lett., Mar, 2003, vol. 1, pp. 6– 9.

[4] N. D. Benavides and P. L. Chapman, “Power budgeting of a multiple input buck-boost converter,” IEEE Trans. Power Electron., vol. 20, no. 6, pp. 1303–1309, Nov. 2005.

[5] H. Matsuo,W. Lin, F. Kurokawa, T. Shigemizu, and N.Watanabe, “Characteristics of the multiple-input DC–DC converter,” IEEE Trans. Ind. Appl., vol. 51, no. 3, pp. 625–631, Jun. 2004.

[6] A. Khaligh, J. Cao, and Y. Lee, “A multiple-input DC–DC converter

[7] Y. M. Chen, Y. C. Liu, and F. Y. Wu, “Multi-input DC/DC converter based on the multiwinding transformer for renewable energy applications,” IEEE Trans. Ind. Appl., vol. 38, no. 4, pp. 1096–1104, Aug. 2002.

[8] A.Kwasinski, “Identification of feasible topologies formultiple-input DCDC converters,” IEEE Trans. Power Electron., vol. 24, no. 3, pp. 856–861, Mar. 2009.

[9] G. Su and L. Tang, “A reduced-part, triple-voltage DC-DC converter for EV/HEV power management,” IEEE Trans. Power Electron., vol. 24, no. 10, pp. 2406–2410, Oct. 2009.

[10] F. Z. Peng, H. Li, G. J. Su, and J. S. Lawler, “A new ZVS bidirectional DC-DC converter for fuel cell and battery applications,” IEEE Trans. Power Electron., vol. 19, no. 1, pp. 54–65, Jan. 2004.

[11] H. Tao, J. L. Duarte, andM. A.M. Hendrix, “Three-port triple-half-bridge bidirectional converter with zero-voltage switching,” IEEE Trans. Power Electron., vol. 23, no. 2, pp. 782–792, Mar. 2008.

[12] W. Jiang and B. Fahimi, “Multi-port power electric interface for renewable energy sources,” in Proc. IEEE Appl. Power Electron. Conf., 2009, pp. 347–352.

[13] D. Liu and H. Li, “A ZVS bi-directional DC-DC converter for multiple energy storage elements,” IEEE

Trans. Power Electron., vol. 21, no. 5, pp. 1513–1517, Sep. 2006.

[14] C. Zhao, S.D.Round, and J.W.Kolar, "An isolated three-port bidirectional DC-DC converter with decoupled power flow management," IEEE Trans. Power Electron., vol. 21, no. 5, pp. 2443–2453, Sep. 2008.

[15] H. Tao, A.Kotsopoulos, J. L.Duarte, andM.A.M.Hendrix, "Transformercoupled multiport ZVS bidirectional DC–DC converter with wide input range," IEEE Trans. Power Electron., vol. 23, pp. 771–781, Mar. 2008.

[16] J. L. Duarte, M. Hendrix, and M. G. Simoes, "Three-port bidirectional converter for hybrid fuel cell systems," IEEE Trans. Power Electron., vol. 22, no. 2, pp. 480–487, Mar. 2007.

[17] H. Al-Atrash and I. Batarseh, "Boost-integrated phase-shift full-bridge converters for three-port interface," in Proc. IEEE Power Electron. Spec. Conf., 2007, pp. 2313–2321.

[18] H. Tao, A. Kotsopoulos, J. L. Duarte, and M. A. M. Hendrix, "Family of multiport bidirectionalDC-DC converters," in Proc. IEEE Power Electron. Spec. Conf., 2008, pp. 796–801.

[19] H. Al-Atrash, F. Tian, and I. Batarseh, "Tri-modal half-bridge converter topology for three-port interface," IEEE Trans. Power Electron., vol. 22, no. 1, pp. 341–345, Jan. 2007.

[20] Z. Qian, O. Abdel-Rahman, J. Reese, H. Al-Atrash, and I. Batarseh, "Dynamic analysis of three-port DC/DC converter for space applications," in Proc. IEEE Appl. Power Electron. Conf., 2009, pp. 28–34.

[21] Z. Qian, O. Abdel-Rahman, M. Pepper, and I. Batarseh, "Analysis and design for paralleled three-portDC/DC converterswith democratic current sharing control," in Proc. IEEE Energy Convers. Congr. Expo., 2009, pp. 1375–1382.

[22] H. Mao, J. Abu-Qahouq, S. Luo, and I. Batarseh, "Zero-voltage-switching half-bridge DC-DC converter with modified PWMcontrolmethod," IEEE Trans. Power Electron., vol. 19, no. 4, pp. 947–958, Jul. 2004.

[23] H. Tao, A. Kotsopoulos, J. L. Duarte, and M. A. M. Hendrix, "Multiinput bidirectional DC-DC converter combining DC-link and magneticcoupling for fuel cell systems," in Proc. IEEE Ind. Appl. Conf., 2005, pp. 2021–2028.

[24] R. W. Erickson and D. Maksimovic, Fundamentals of Power Electronics, 2nd ed. Boston, MA: Kluwer, 2000, ch. 7.

[25] H. Al-Atrash, M. Pepper, and I. Batarseh, "A zero-voltage switching three-port isolated full-bridge converter," in Proc. IEEE Int. Telecommun. Energy Conf., 2006, pp.411–418.

[26] Z. Qian, O. Abdel-Rahman, H. Hu, and I. Batarseh, "Multi-channel threeport DC/DC converters as maximal power tracker, battery charger and bus regulator," in Proc. IEEE Appl. Power Electron. Conf., 2010, pp. 2073–2079.

[27] H. Krishnaswami and N. Mohan, "Three-port series-resonant DC–DCconverter to interface renewable energy sources with bidirectional load and energy storage ports," IEEE Trans. Power Electron., vol. 24, no. 9–10, pp. 2289–2297, Oct. 2009.

[28] Z. Qian, O. Abdel-Rahman, H. Al-trash, and I. Batarseh, "Modeling and control of three-port DC/DC converter interface for satellite applications, IEEE Trans. Power Electron., vol. 25, no. 3, pp. 637–649, Mar. 2010.